AGU PUBLICATIONS

Geophysical Research Letters

RESEARCH LETTER
10.1002/2015GL065423

Key Points:
- We characterize a double porosity transport model from pore-scale rock images
- We employ the full pdf of pore-scale velocities to quantify model parameters
- Our model predicts transport within real porous media with high fidelity

Supporting Information:
- Texts S1–S3, Figures S2 and S3, and Tables S2 and S3

Correspondence to:
G. M. Porta,
giovanni.porta@polimi.it

Citation:
Porta, G. M., B. Bijeljic, M. J. Blunt, and A. Guadagnini (2015), Continuum-scale characterization of solute transport based on pore-scale velocity distributions, *Geophys. Res. Lett.*, *42*, doi:10.1002/2015GL065423.

Received 17 JUL 2015
Accepted 21 AUG 2015
Accepted article online 25 AUG 2015

Continuum-scale characterization of solute transport based on pore-scale velocity distributions

G. M. Porta[1], B. Bijeljic[2], M. J. Blunt[1,2], and A. Guadagnini[1,3]

[1]Dipartimento di Ingegneria Civile e Ambientale, Politecnico di Milano, Milano, Italy, [2]Department of Earth Science and Engineering, Imperial College, London, UK, [3]Department of Hydrology and Water Resources, University of Arizona, Tucson, Arizona, USA

Abstract We present a methodology to characterize a continuum-scale model of transport in porous media on the basis of pore-scale distributions of velocities computed in three-dimensional pore-space images. The methodology is tested against pore-scale simulations of flow and transport for a bead pack and a sandstone sample. We employ a double-continuum approach to describe transport in mobile and immobile regions. Model parameters are characterized through inputs resulting from the micron-scale reconstruction of the pore space geometry and the related velocity field. We employ the outputs of pore-scale analysis to (i) quantify the proportion of mobile and immobile fluid regions and (ii) assign the velocity distribution in an effective representation of the medium internal structure. Our results (1) show that this simple conceptual model reproduces the spatial profiles of solute concentration rendered by pore-scale simulation without resorting to model calibration and (2) highlight the critical role of pore-scale velocities in the characterization of the model parameters.

1. Introduction

Recent advances in image processing and direct flow simulation enable us to characterize with high fidelity the details of the pore-scale geometry and the velocity field within complex three-dimensional porous media [e.g., *Spanne et al*., 1994; *Bijeljic et al*., 2013a, 2013b; *Siena et al*., 2014; *Scheibe et al*., 2015]. Results of computational analyses of pore-scale solute transport on imaged pore spaces have been validated against nuclear magnetic resonance (NMR) experiments in terms of probability distributions of particle displacements [*Bijeljic et al*., 2013a; *Scheven et al*., 2005]. These studies have opened up opportunities to quantitatively assess the way this wealth of pore-scale information can be incorporated into continuum-scale models. This work explicitly addresses this point. The conceptual and operational framework we consider is especially relevant to applications associated with large-scale flow and transport, where effective transport models are needed to predict and understand macroscale phenomena.

A classical continuum approach to model transport in porous media relies on the use of the classical advection dispersion equation (ADE). A key assumption underlying the ADE is that pore-scale dynamics can be projected onto a continuum-scale model through a Fickian analogy. Limitations of this assumption have been convincingly demonstrated through theoretical, numerical, and experimental arguments [e.g., *Salles et al*., 1993; *Auriault and Adler*, 1995; *Berkowitz et al*., 2000; *Bijeljic and Blunt*, 2006]. A variety of approaches have then been developed to interpret observations of seemingly non-Fickian solute transport observed at laboratory and field scales [e.g., *Zhang et al*., 2009; *Berkowitz et al*., 2006; *Haggerty et al*., 2004]. All these effective formulations typically include a set of model parameters. While these must be related to pore-scale velocity and geometry, they typically need to be estimated through fitting against solute concentration data, e.g., measured breakthrough curves. Recent studies have shown that it is possible to link the nature of effective parameters capturing non-Fickian behavior to results obtained by Lagrangian effective models based on simulated pore-scale flow characteristics [*De Anna et al*., 2013; *Kang et al*., 2014].

Here we present a double-continuum (or two-region) model of transport and explicitly link model parameters to the pore-scale velocity field. We conceptualize the porous medium as composed by two overlapping effective continua, respectively constituting a mobile and an immobile region [e.g., *Coats and Smith*, 1964]. The nature of transport is typically considered to be diffusive in the immobile region, while advection and dispersion drive solute displacement in the mobile region. While this continuum-scale model is widely used, quantitative characterization of effective model parameters relying on pore-scale quantities associated with real three-dimensional rock samples is still lacking. In this context, *Swanson et al*. [2015] have shown that relying solely

on information about the geometrical attributes of the pore space obtained through NMR and electric resistivity measurements does not lead to a reliable characterization of the full set of model parameters.

Parameters of double-continuum models can directly be related to pore-scale features by theoretical studies based on volume averaging [e.g., *Davit et al.*, 2010; *Orgogozo et al.*, 2010; *Davit et al.*, 2012; *Soulaine et al.*, 2013; *Porta et al.*, 2013]. Rigorous application of volume averaging to real porous media requires solving a set of closure problems in a (generally) complex three-dimensional geometry. This is a demanding task from an implementation and computational perspective. Thus, it is also useful to develop more simplified approaches.

Here we present a straightforward methodology to directly embed into the parameters of a two-region (double-continuum) model flow field information from complex three-dimensional pore spaces derived from micron-resolution images of rock samples. Our work uses velocity fields which have been directly calculated in the pore space and validated through comparison with NMR experiments [*Bijeljic et al.*, 2013a]. We demonstrate the critical role of the knowledge of the pore-scale velocity field for an accurate effective description of transport at the continuum scale.

2. Modeling Approach

We provide here a characterization of the pore spaces we consider and a brief description of our modeling approach.

2.1. Pore-Scale Characterization

We consider transport of a nonreactive solute through a single-phase flow field in a three-dimensional porous domain, Ω. The latter comprises a solid (Ω_S) and a liquid (Ω_L) phase. We assume that transport in Ω_L is described by an advection-diffusion equation:

$$\frac{\partial \hat{c}_{PS}}{\partial \hat{t}} + \hat{\mathbf{u}}_{PS}\hat{\nabla}\hat{c}_{PS} = \hat{D}_m\hat{\nabla}^2\hat{c}_{PS}; \qquad \hat{\mathbf{x}}\in\Omega_L, \tag{1}$$

where $\hat{c}_{PS}$ (mol m^{-3}) is pore-scale concentration, $\hat{\mathbf{x}}$ is the spatial coordinate vector, $\hat{t}$ is time, $\hat{\mathbf{u}}_{PS}(\hat{\mathbf{x}})$ (m s^{-1}) is fluid velocity within the pore space, and $\hat{D}_m$ (m^2 s^{-1}) is molecular diffusion. Here and in the following all hat-signed variables are dimensional.

We study transport in two three-dimensional samples, a bead pack and a Bentheimer sandstone image, each comprising 300^3 voxels, with voxel size of 2 and 3 μm, respectively. Porosity, ϕ, is equal to 35.9% and 21.5%, respectively, for the bead pack and sandstone sample. Pore space geometries and the velocity fields $\hat{\mathbf{u}}_{PS}(\hat{\mathbf{x}})$ are obtained at the resolution of the voxel size for each medium [*Bijeljic et al.*, 2013a]. Details on the characterization of the bead pack and sandstone samples at the pore scale and image segmentation are provided in [*Bijeljic et al.*, 2013a; *Guadagnini et al.*, 2014] and are summarized in the supporting information Text S1.

Fluid velocities on image voxels are obtained by solving the steady state Navier-Stokes equations for incompressible single-phase Newtonian flow. The velocity and pressure fields are computed through the numerical solver implemented in OpenFOAM [*Bijeljic et al.*, 2013a; *Raeini et al.*, 2012; *OpenFOAM*, 2011]. A constant pressure difference is assigned between the inlet and outlet faces of the image along the x direction. Details on the pore-scale computations including the key equations, meshing, and convergence criteria are provided in supporting information Text S2.

Pore-scale transport is simulated by particle tracking [*Bijeljic et al.*, 2011]. We initially place 10^7 particles at random within the pore space. The total displacement $\hat{\mathbf{x}}_{\text{tot}}$ of particles within a given time step $d\hat{t}$ is computed as $\hat{\mathbf{x}}_{\text{tot}} = \hat{\mathbf{x}}_{\text{adv}} + \hat{\mathbf{x}}_{\text{diff}}$, where $\hat{\mathbf{x}}_{\text{adv}}$ is the advective displacement calculated semianalytically along the streamlines using a modified Pollock algorithm [*Pereira Nunes et al.*, 2015] and $\hat{\mathbf{x}}_{\text{diff}} = \sqrt{24\hat{D}_m d\hat{t}}(R-0.5)$ is the diffusive displacement, R being a random number uniformly distributed between 0 and 1 [*Benson and Meerschaert*, 2008].

Appropriate reflection boundary conditions at solid voxels are imposed [*Bijeljic et al.*, 2011]. When particles hit solid voxels within $d\hat{t}$, they are bounced back to the pore voxels in a random direction and traverse the remainder of the diffusive displacement until the end of $d\hat{t}$ [*Bijeljic et al.*, 2011]. Particles exiting from the imaged pore space along the x direction are reinjected into the system from the inlet face.

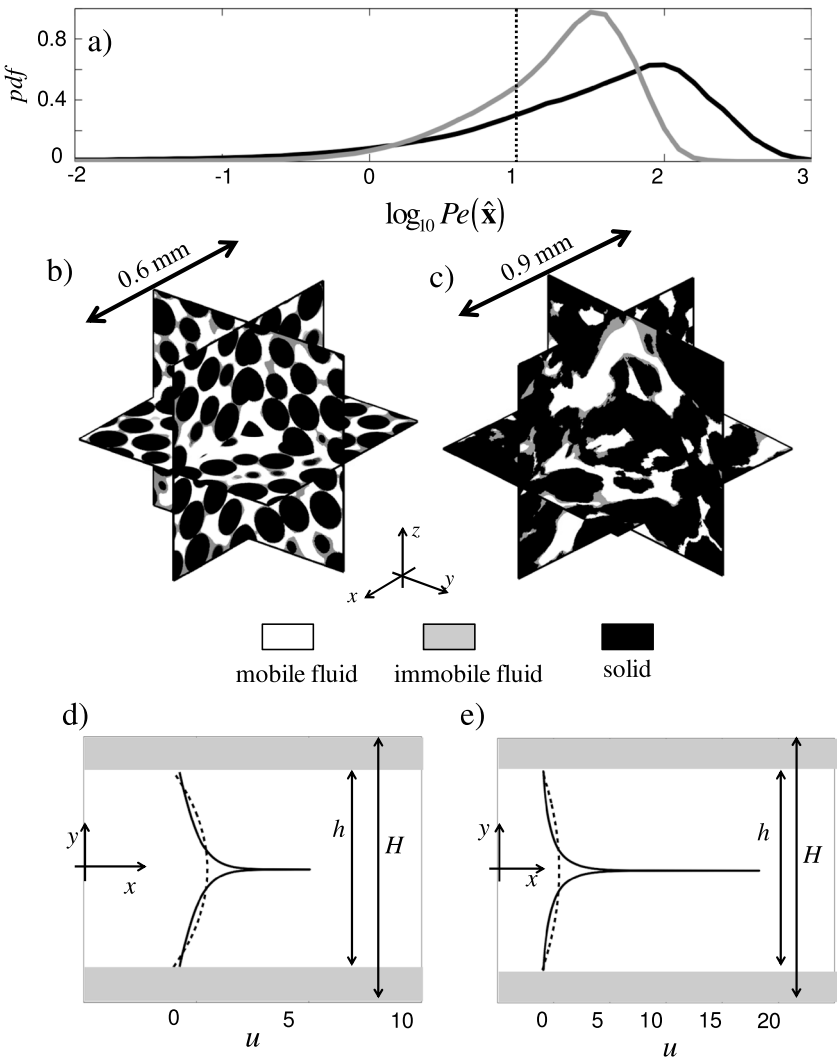

Figure 1. Model characterization: (a) sample pdf of $\log_{10} Pe(\hat{\mathbf{x}})$ for bead pack (gray curve) and Bentheimer sandstone (black curve); spatial distribution of solid (black shaded area), immobile (gray shaded area) and mobile (white area) fluid regions within the (b) bead pack and (c) sandstone samples; unit cell models for (d) bead pack and (e) sandstone with associated velocity distributions for model 1 (dashed lines) and model 2 (continuous lines). In Figure 1a the dash-dotted line indicates the value $Pe(\hat{\mathbf{x}}) = Pe_{thr} = 10$.

As in *Porta et al.* [2013], we define the local Péclet number:

$$Pe(\hat{\mathbf{x}}) = \frac{|\hat{\mathbf{u}}_{PS}(\hat{\mathbf{x}})|\hat{L}}{\hat{D}_m} \tag{2}$$

which is the ratio of the time scales characterizing transport by advection and diffusion across a characteristic length scale $\hat{L}$ (m). As in *Bijeljic et al.* [2013a], the velocity fields $\hat{\mathbf{u}}_{PS}(\hat{\mathbf{x}})$ are computed in the two media such that the average velocity $\hat{U}$ along the x direction is equal to 0.91×10^{-3} m/s and 1.02×10^{-3} m/s for the bead pack and sandstone samples, respectively, corresponding to Reynolds number $Re = 5.2 \times 10^{-2}$ and $Re = 1.25 \times 10^{-1}$. The molecular diffusion coefficient $\hat{D}_m$ is set equal to 2.2×10^{-9} m^2/s. This set of parameters has been used in *Bijeljic et al.* [2013a] to replicate the experimental conditions for measurements of transport obtained by NMR in the same porous samples [*Scheven et al.*, 2005]. We consider the length scale $\hat{L}$ as an average pore size. We set $\hat{L} = 56\,\mu$m for the bead pack, according to the formulation $\hat{L} = \hat{d}_G\phi/(1-\phi)$ [*Whitaker*, 1999], where $\hat{d}_G = 100\,\mu$m is the uniform diameter of the spheres forming the bead pack. In the absence of a corresponding theoretical formulation, we estimate $\hat{L}$ for the sandstone sample as the range of the variogram of the indicator function $G(\mathbf{x})$ ($G(\mathbf{x}) = 0$ for solid grains and $G(\mathbf{x}) = 1$ for fluid) resulting from

pore-scale imaging. We do so by employing an exponential model to interpret the variogram reported by *Bijeljic et al.* [2013a] and estimate $\hat{L} = 121\,\mu m$. We then obtain average values of the Péclet number $Pe_{av} = \hat{U}\hat{L}/\hat{D}_m = 23.2$ and 56.4, respectively, for the bead pack and the sandstone.

Figure 1a depicts the sample probability density function (pdf) of the decimal logarithm of $Pe(\hat{\mathbf{x}})$ for the two media. The pdf associated with the sandstone medium reflects the occurrence of a wider variability of $Pe(\hat{\mathbf{x}})$ as compared to the bead pack sample.

The three-dimensional map of $Pe(\hat{\mathbf{x}})$ explicitly identifies low-velocity regions where advective transport takes place over time scales which are considerably longer than those associated with molecular diffusion. We demarcate mobile (advection dominated, Ω_M) and immobile (diffusion dominated, Ω_I) zones, with $\Omega_M \cup \Omega_I = \Omega_L$, by setting $\Omega_M = \{\hat{\mathbf{x}} \in \Omega_L : Pe(\hat{\mathbf{x}}) > Pe_{thr}\}$ and $\Omega_I = \{\hat{\mathbf{x}} \in \Omega_L : Pe(\hat{\mathbf{x}}) < Pe_{thr}\}$, where Pe_{thr} is a preset threshold value.

As an example, Figure 1b, c depicts the spatial arrangement of Ω_M and Ω_I within the two media for $Pe_{thr} = 10$. In both systems we observe a thin layer of immobile fluid around the solid grains. The bead pack exhibits a regular structure and immobile portions of the pore space appear to be uniformly dispersed within Ω_L (Figure 1b). The sandstone sample is characterized by wider and more localized low-velocity regions (Figure 1c). In these examples the mobile fraction of the pore space, $\gamma_M = |\Omega_M|/|\Omega_L|$, is approximately the same (≈0.75) for both media.

2.2. Continuum-Scale Modeling of Transport

We illustrate here our approach to employ the pore-scale velocity field computed in a pore space image to characterize an effective continuum-scale transport model. To this end, we incorporate the richness of the velocity information resulting from the pore-scale characterization introduced in section 2.1 into a simplified conceptual model of the porous medium geometry.

We conceptualize the porous system as an elementary cell, which corresponds to an equivalent fluid volume comprised between two parallel plates separated by a uniform aperture of width $\hat{H}$ (see Figures 1d–1e). We assume that the total fluid volume within the two parallel plates is subdivided into a mobile region of width $\hat{h}$, associated with a given velocity distribution (directed along the x axis, see Figures 1d–1e), and an immobile region of total width $(\hat{H} - \hat{h})$, where velocity is set to zero. This partition, i.e., the value of $\hat{h}$, is calculated from the distribution of $Pe(\hat{\mathbf{x}})$ that is obtained from the characterization of flow at the pore-scale, as described in section 2.1, and the selected threshold value, Pe_{thr}. While our conceptual model relies on a simplification of the actual pore space, it enables us to derive simple analytical formulations for the double-continuum model parameters. Our approach is also consistent with previous findings showing that this simplified geometry can provide powerful guidance for the interpretation of flow and transport phenomena taking place in complex pore spaces [e.g., *Davit et al.*, 2010; *Orgogozo et al.*, 2010; *Wang et al.*, 2012; *Porta et al.*, 2013; *Dejam et al.*, 2014; *Bianchi Janetti et al.*, 2015]. We now discuss the key developments leading to the definition of our effective transport models. All details are presented as supporting information Text S3. We assume that solute concentration dynamics are described via the dimensionless formulation:

$$\frac{\partial M}{\partial t} + u\frac{\partial M}{\partial x} = \frac{1}{Pe}\nabla^2 M \qquad |y| < h/2 \tag{3}$$

$$\frac{\partial I}{\partial t} = \frac{1}{Pe}\nabla^2 I \qquad |y| > h/2 \tag{4}$$

Here $M = \hat{M}/\hat{c}_0$ and $I = \hat{I}/\hat{c}_0$ are dimensionless concentrations in the mobile and immobile regions, respectively, $\hat{c}_0$ being a characteristic concentration typically related to initial or boundary conditions; $t = \hat{t}\hat{H}/\hat{U}_M$ is dimensionless time; $\mathbf{x} = \hat{\mathbf{x}}/\hat{H}$; $h = \hat{h}/\hat{H}$; $u = \hat{u}/\hat{U}_M$ is velocity along the x direction where $\hat{U}_M$ is the average velocity in the mobile region; and $Pe = \hat{U}_M\hat{H}/\hat{D}_m$. Note that $\hat{U}_M = \hat{U}/\gamma_M$ and $Pe = Pe_{av}/\gamma_M$. Equations (3) and (4) are completed by the boundary conditions:

$$M = I, \quad \frac{\partial M}{\partial y} = \frac{\partial I}{\partial y} \quad |y| = h/2; \quad \frac{\partial I}{\partial y} = 0 \quad |y| = H/2 = 1/2; \quad H = \hat{H}/\hat{H} = 1 \tag{5}$$

ensuring that solute flux is continuous across the mobile-immobile interface and imposing zero flux at the fluid-solid boundary.

Averaging (3) and (4) along the system cross-sectional area normal to the mean flow direction yields:

$$\frac{\partial \overline{M}}{\partial t}+\frac{\partial \overline{M}}{\partial x}+\frac{\partial \overline{\widetilde{u}\widetilde{M}}}{\partial x}=\frac{1}{Pe}\frac{\partial^2 \overline{M}}{\partial x^2}+\frac{2}{Peh}\frac{\partial \widetilde{M}}{\partial y}\bigg|_{y=h/2} \tag{6}$$

$$\frac{\partial \overline{I}}{\partial t}=\frac{1}{Pe}\frac{\partial^2 \overline{I}}{\partial x^2}-\frac{2}{Pe(1-h)}\frac{\partial \widetilde{I}}{\partial y}\bigg|_{y=h/2} \tag{7}$$

where $\overline{M}$ and $\overline{I}$ are section-averaged concentrations in the mobile and immobile regions, $\widetilde{M}=M-\overline{M}$ and $\widetilde{I}=I-\overline{I}$ are the associated deviations, and $\widetilde{u}=u-U_M$. Equations (6) and (7) can be expressed in closed form by relating the concentration deviations to section-averaged quantities. We do so by introducing the following closure relationships (see supporting information Text S3 for details):

$$\widetilde{M}=b_1(y)\frac{\partial \overline{M}}{\partial x}+b_3(y)\Delta\overline{c};\qquad \widetilde{I}=b_2(y)\frac{\partial \overline{M}}{\partial x}+b_4(y)\Delta\overline{c} \tag{8}$$

where $b_i(y)$ ($i=1,\cdots,4$) are closure variables and $\Delta\overline{c}=\overline{M}-\overline{I}$. Closure (8) stems from a generalization of the classical Taylor-Aris theory of dispersion to the double region unit cells depicted in Figures 1d–1e. In this context the drivers of transport in the two-region model are the longitudinal gradient of concentration (as in the classical Taylor-Aris analysis) and the difference between concentrations in the mobile and immobile regions (as in a standard double-continuum approach). Upon replacing (8) into (6) and (7), the closed form of the section-averaged system reads:

$$\frac{\partial \overline{M}}{\partial t}+\frac{\partial \overline{M}}{\partial x}+\frac{\partial}{\partial x}\left[d_{H1}\frac{\partial \overline{M}}{\partial x}+d_{H2}\Delta\overline{c}\right]=\frac{1}{Pe}\frac{\partial^2 \overline{M}}{\partial x^2}+\frac{1}{Pe\gamma_M}\left(e_1\frac{\partial \overline{M}}{\partial x}+e_2\Delta\overline{c}\right) \tag{9}$$

$$\frac{\partial \overline{I}}{\partial t}=\frac{1}{Pe}\frac{\partial^2 \overline{I}}{\partial x^2}-\frac{1}{Pe\gamma_I}\left(e_1\frac{\partial \overline{M}}{\partial x}+e_2\Delta\overline{c}\right) \tag{10}$$

where $\gamma_I=|\Omega_I|/|\Omega_L|$, i.e., $\gamma_M+\gamma_I=1$, and the model effective parameters are defined as

$$d_{H1}=\frac{1}{h}\int_{-h/2}^{h/2}b_1\widetilde{u}\,dy;\qquad d_{H2}=\frac{1}{h}\int_{-h/2}^{h/2}b_3\widetilde{u}\,dy;\qquad e_1=2\frac{\partial b_2}{\partial y}\bigg|_{y=h/2};\qquad e_2=2\frac{\partial b_4}{\partial y}\bigg|_{y=h/2} \tag{11}$$

The effective parameters (11) are computed within the unit cell from the distribution of $\widetilde{u}$ along the y direction. We consider the effect of the following two strategies to characterize $\widetilde{u}$:

1. Model 1: we assume Poiseuille flow (i.e., a parabolic velocity profile) in the mobile region. The corresponding dimensionless velocity distribution is depicted in Figures 1d–1e for the two samples considered. In both cases $u(y)$ attains a maximum value of 1.5 for $y=0$ (Figures 1d–1e);
2. Model 2: we set the shape of the velocity distribution in the upper and lower half of the mobile region as coinciding with the (appropriately rescaled) sample cumulative distribution function (cdf) of pore-scale velocities, as depicted in Figures 1d–1e. We consider a truncated cdf of velocity by using only values of velocities associated with local Péclet number above the threshold Pe_{thr} (i.e., within Ω_M). As a consequence, the velocity distribution attains a minimum value $u_{min}=Pe_{thr}\hat{U}_M\hat{D}_m/\hat{L}>0$ at the mobile-immobile boundary ($|y|=h/2$). The velocity distributions corresponding to the two samples are depicted in Figures 1d–1e. Note that while the average velocity value is equal to one for both systems, velocities in the sandstone sample display a wider range of variability, the largest (dimensionless) velocity value approaching 20 (see Figure 1d), as opposed to a value of approximately 5 for the bead pack (Figure 1e).

The coefficients (11) are analytically known for model 1, while they are computed numerically for model 2 (see supporting information Text S3 and Table S2). Models 1 and 2 embed pore-scale information to a different extent: the former takes into account pore-scale information solely to partition the pore space into mobile and immobile regions; the latter also considers the full sample distribution of velocities for the evaluation of the model effective parameters, albeit lumped into a simplified format and geometry. Model 2 views effective transport as taking place in a single representative pore within which the full distribution of velocity computed at the pore-scale is considered to be present and is employed to directly compute model parameters (11). As opposed to other techniques [*Kang et al.*, 2014], our model disregards velocity correlations along particle trajectories and does not require a characterization of the spatially heterogeneous structure associated with

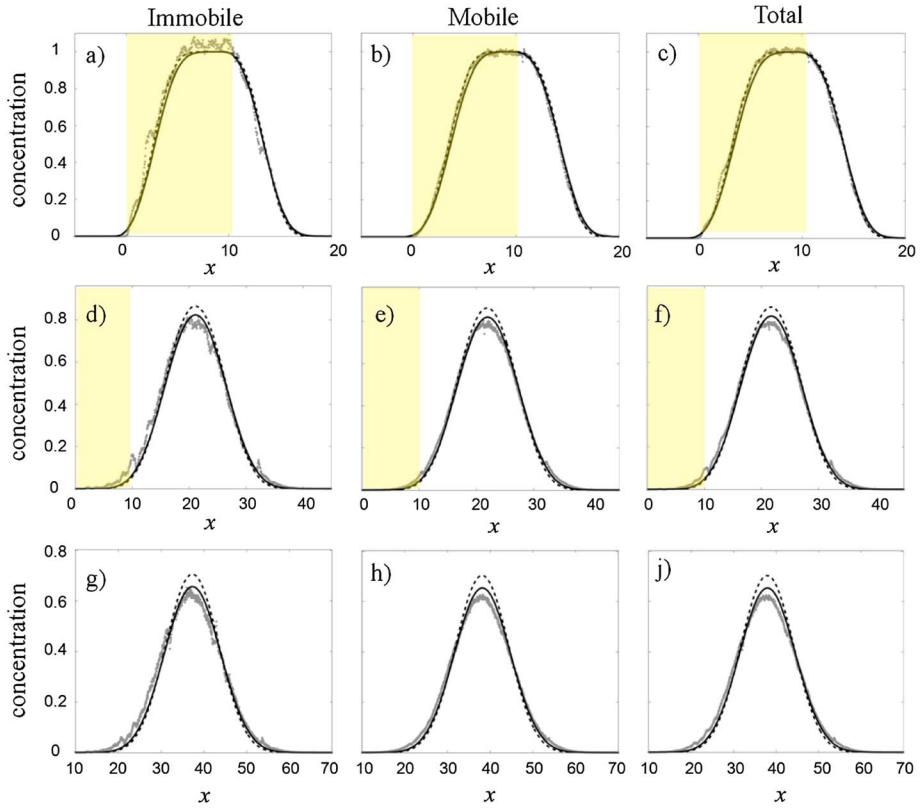

Figure 2. Bead pack sample: comparison of section-averaged (a, d, and g) immobile, (b, e, and h) mobile, and (c, f, and j) total concentrations yielded by pore-scale particle tracking (gray points), model 1 (dashed curve) and model 2 (continuous curve). Results are for $t = 4.6$ (Figures 2a–2c), 22.7 (Figures 2a–2c), 45.4 (Figures 2d–2f); the shaded area in Figures 2a–2f indicates the interval $0 < x < x_0$ where the solute is initially placed.

pore-scale velocity and geometry. This is consistent with the results by *Bolster et al.* [2014] which show that correlation effects are not relevant for $Pe_{av} < 100$. Diffusion drives mixing at the pore scale for small Péclet numbers (e.g., $Pe_{av} < 10$) and concentration differences between mobile and immobile regions become typically negligible after a short distance is traveled by solute particles. Therefore, we test here our model in the regime $10 < Pe_{av} < 100$ for which the mass transfer process is expected to play some role, particularly for early times.

Note that in both models effective parameters are influenced by the choice of Pe_{thr}, i.e., by the criterion employed to quantify γ_M. In the following we set $Pe_{thr} = 10$ to illustrate our results; we have verified that the selected threshold value has a limited impact on the results illustrated in section 3 within the interval $1 \leq Pe_{thr} \leq 10$ (see supporting information Text S3).

3. Results

We compare the results obtained by direct pore-scale simulations in the imaged pore spaces (see section 2.1) against those rendered by the double-continuum formulations outlined in section 2.2. In the pore-scale simulations solute particles are initially placed within a given volume of the porous domain to mimic an initial constant concentration $\hat{c}_0$. We represent this initial condition by setting $M = \hat{M}/\hat{c}_0 = 1$ and $I = \hat{I}/\hat{c}_0 = 1$ within the interval $0 < x < x_0$, with $x_0 = \hat{L}_{\text{image}}/\hat{L}$, $\hat{L}_{\text{image}}$ being the total length of the image of the porous medium (i.e., $x_0 = 10.7$ or 7.4, respectively, for the bead pack and the sandstone). The solutions of the double-continuum formulation associated with models 1 and 2 are obtained by solving the one-dimensional formulation (9) and (10) through the Matlab function "pdepe".

Figure 2 depicts the longitudinal (along direction x) concentration profiles obtained for the bead pack sample at dimensionless times $t = 4.6$ (Figures 2a–2c), 22.7 (Figures 2d–2f), and 45.7 (Figures 2g–2j), corresponding to dimensional times $\hat{t} = 0.2,\ 1.0,\ 2.0$ s. We compare section-averaged concentrations in the immobile

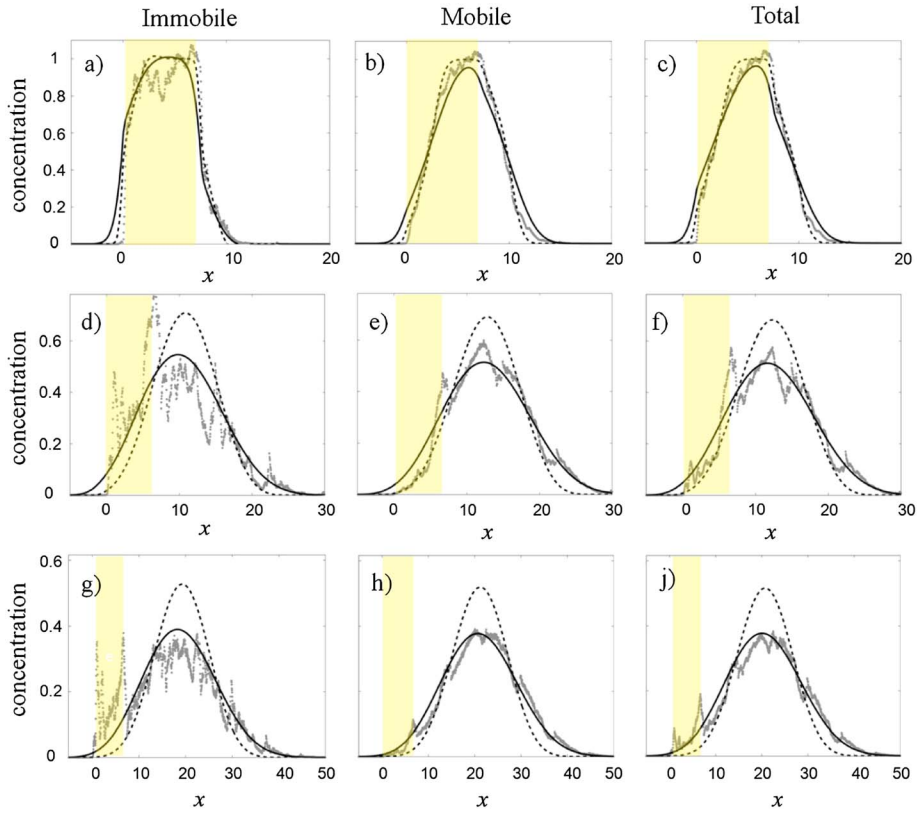

Figure 3. Sandstone sample: comparison of section-averaged (a, d, and g) immobile, (b, e, and h) mobile, and (c, f, and j) total concentrations as yielded by pore-scale particle tracking (gray points), model 1 (dashed curve), and model 2 (continuous curve). Results are for $t = 2.2$ (Figures 3a–3c), 11.2 (Figures 3d–3f), and 22.4 (Figures 3g–3j); the shaded area indicates the interval $0 < x < x_0$ where the solute is initially placed.

(Figures 2a, 2d, and 2g) and mobile (Figures 2b, 2e, and 2h) regions as well as total concentrations (Figures 2c, 2f, and 2j), obtained as $c = \gamma_M M + \gamma_I I$. The concentration profiles appear to be symmetric and are characterized by similar shapes in the mobile and immobile regions. As time advances, model 1 overestimates the concentration peak and underestimates concentrations at the forward and backward tails. Employing model 2 leads to results of improved quality when compared to model 1 (see Figures 2c, 2f, and 2j).

Figure 3 illustrates the results obtained for the sandstone medium for $t = 2.2$ (Figures 3a–3c), 11.2 (Figures 3d–3f), and 22.4 (Figures 3g–3j), corresponding to the same dimensional times considered for the bead pack. Effective model results for $t = 2.2$ display a good agreement with pore-scale simulations (Figures 3a–3c). For longer times model 2 is able to reproduce the total concentration profiles stemming from pore-scale simulation (see Figures 3f and 3j), while model 1 underestimates solute spreading along the longitudinal direction.

We quantify the modeling error associated with models 1 and 2 when compared against pore-scale simulations in Figure 4a, where we consider the time evolution of:

$$E_{L2}(t) = \frac{\int_L [c(x,t) - c_{PS}(x,t)]^2 \mathrm{d}x}{\int_L c_{PS}^2(x,t)\mathrm{d}x} \tag{12}$$

which corresponds to the relative L^2-norm of the error between continuum-scale predictions, c, and pore-scale results, c_{PS}. As an additional metric, Figure 4b depicts the temporal evolution of the dilution index [*Kitanidis*, 1994]:

$$DI(t) = \frac{1}{x_0}\int_L p(x,t)\ln[p(x,t)]\mathrm{d}x; \qquad p(x,t) = \frac{c(x,t)}{\int_L c(x,t)\mathrm{d}x} \tag{13}$$

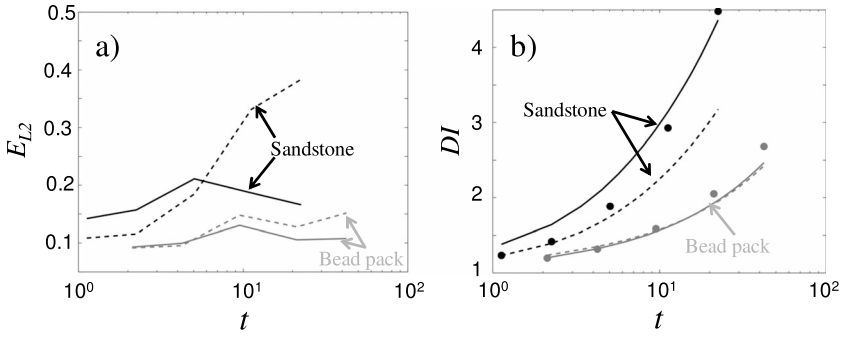

Figure 4. Temporal evolution of (a) the relative error (12) and (b) the dilution index (13) for bead pack (gray curves and symbols) and sandstone (black curves and symbols). Results are obtained by continuum effective models 1 (dashed lines) and 2 (continuous lines) and pore-scale simulations (symbols in Figure 4b).

which quantifies the length of the solute plume along the x direction. To obtain comparable results between the bead pack and sandstone sample, we rescale $DI(t)$ by x_0, as the solute is initially distributed over a volume of length equal to x_0 in the two samples.

For the bead pack sample, both models display similar relative errors for $t < 10$. For longer times, the error related to model 2 is relatively stable and equal to about 10%, while the error associated with model 1 increases up to 15% (see the gray curves in Figure 4a). These results reflect the improved ability of model 2 to provide robust estimates of the concentration peak (see Figures 2f and 2j). Figure 4b suggests that the two continuum-scale models predict approximately the same temporal evolution of the dilution index for the bead pack. We observe that both models underestimate dilution observed by pore-scale simulation by approximately 10% for the longest time considered ($t = 45$).These results indicate that the assumed velocity distribution has a limited impact on a global metric expressing the dilution of the solute while being mildly relevant to the proper prediction of the solute distribution along x.

Continuum scale predictions for the sandstone sample are less accurate than those obtained for the bead pack sample (see Figure 4a). This result is explained by considering the irregular behavior of concentration profiles resulting from the pore-scale simulation (see Figure 3). This is chiefly due to the spatially heterogeneous structure of velocity and geometry at the pore level. The temporal evolutions of both the modeling error and the dilution index show that for short times ($t < 5$) model 1 is slightly more accurate than model 2 (see Figures 4a and 4b). However, as time progresses the error associated with model 1 increases up to 40% for $t = 22.4$ while remaining at approximately 15% for model 2. Moreover, model 1 largely underestimates the dilution index for $t > 5$, consistent with the quality of predictions observed for the concentration profiles (see Figures 3f and 3j). The error associated with model 2 for short times might be related to nonlocal effects resulting from the transient behavior of transport parameters, which are disregarded in our approach (see supporting information Text S3). By accounting for the full distribution of the pore-scale velocity, model 2 predicts the dilution index up to an accuracy of 15% at $t = 22.4$ (see Figure 4b).

4. Conclusions

We provide predictions of solute transport within explicit pore spaces associated with two three-dimensional porous media, a bead pack, and a consolidated sandstone. We base our results on a modeling approach which describes the porous medium through a simple system which is formed by two parallel plates and directly exploits information on the pdf of the pore-scale velocities for the characterization of the parameters of an effective one-dimensional double-continuum (two-region) model. In essence, our methodology involves the followings: (1) replacing the porous medium with the simplified conceptual model illustrated above, based on the information resulting from pore-scale simulation of flow; (2) computing the effective parameters of transport within a unit cell by solving a one-dimensional closure problem; and (3) solving the continuum-scale transport problem. Our results indicate that even in its simplicity, our conceptual model can lead to accurate (with a relative error lower than 15% with respect to results from direct pore-scale simulations) characterization of longitudinal solute dilution in the two systems analyzed when the critical role of pore-scale velocities is taken into account.

Acknowledgments
G.M.P. and A.G. acknowledge financial support of MIUR (Projects PRIN 2010/2011 "Hydroelectric energy by osmosis in coastal areas" and "Innovative methods for water resources under hydro-climatic uncertainty scenarios"). B.B. and M.J.B. wish to thank the Engineering and Physical Science Research Council for the financial support through grant EP/L012227/1. The data used to produce the results of this paper are freely available upon request to the corresponding author.

The Editor thanks two anonymous reviewers for their assistance in evaluating this paper.

References

Auriault, J.-L., and P. M. Adler (1995), Taylor dispersion in porous media: Analysis by multiple scale expansions, *Adv. Water Resour.*, *18*, 217–226.
Benson, D. A., and M. M. Meerschaert (2008), Simulation of chemical reaction via particle tracking: Diffusion-limited versus thermodynamic rate-limited regimes, *Water Resour. Res.*, *44*, W12201, doi:10.1029/2008WR007111.
Berkowitz, B., H. Scher, and S. E. Silliman (2000), Anomalous transport in laboratory-scale, heterogeneous porous media, *Water Resour. Res.*, *36*, 149–158, doi:10.1029/1999WR900295.
Berkowitz, B., A. Cortis, M. Dentz, and H. Scher (2006), Modeling non-Fickian transport in geological formations as a continuous time random walk, *Rev. Geophys.*, *44*, RG2003, doi:10.1029/2005RG000178.
Bianchi Janetti, E., M. Riva, and A. Guadagnini (2015), Three-phase permeabilities: upscaling, analytical solutions and uncertainty analysis in elementary pore structures, *Transp. Porous Media*, *106*, 259–283.
Bijeljic, B., and M. J. Blunt (2006), Pore-scale modeling and continuous time random walk analysis of dispersion in porous media, *Water Resour. Res.*, *42*, W01202, doi:10.1029/2005WR004578.
Bijeljic, B., P. Mostaghimi, and M. J. Blunt (2011), Signature of non-Fickian solute transport in complex heterogeneous porous media, *Phys. Rev. Lett.*, *107*, 204502.
Bijeljic, B., A. Raeini, P. Mostaghimi, and M. J. Blunt (2013a), Predictions of non-Fickian solute transport in different classes of porous media using direct simulation on pore-scale images, *Phys. Rev. E*, *87*, 013011, doi:10.1103/PhysRevE.87.013011.
Bijeljic, B., P. Mostaghimi, and M. J. Blunt (2013b), Insights into non-Fickian solute transport in carbonates, *Water Resour. Res.*, *49*, 2714–2728, doi:10.1002/wrcr.20238.
Bolster, D., Y. Méheust, T. Le Borgne, J. Bouquain, and P. Davy (2014), Modeling preasymptotic transport in flows with significant inertial and trapping effects—The importance of velocity correlations and a spatial Markov model, *Adv. Water Resour.*, *70*, 89–103.
Coats, K. H., and B. D. Smith (1964), Dead-end pore volume and dispersion in porous media, *Soc. Pet. Eng. J.*, *4*, 73–84.
Davit, Y., M. Quintard, and G. Debenest (2010), Equivalence between volume averaging and moments matching techniques for mass transport models in porous media, *Int. J. Heat Mass Trans.*, *53*(21), 4985–4993.
Davit, Y., B. D. Wood, G. Debenest, and M. Quintard (2012), Correspondence between one-and two-equation models for solute transport in two-region heterogeneous porous media, *Trans. Porous Media*, *95*(1), 213–238.
de Anna, P., T. Le Borgne, M. Dentz, A. M. Tartakovsky, D. Bolster, and P. Davy (2013), Flow intermittency, dispersion, and correlated continuous time random walks in porous media, *Phys. Rev. Lett.*, *110*, 184502.
Dejam, M., H. Hassanzadeh, and Z. Chen (2014), Shear dispersion in a fracture with porous walls, *Adv. Water Resour.*, *74*, 14–25.
Guadagnini, A., M. J. Blunt, M. Riva, and B. Bijeljic (2014), Statistical scaling of geometric characteristics in millimeter scale natural porous media, *Transp. Porous Media*, *101*, 465–475, doi:10.1007/s11242-013-0254-7.
Haggerty, R., C. F. Harvey, C. F. von Schwerin, and L. C. Meigs (2004), What controls the apparent timescales in aquifers and soils? A comparison of experimental results, *Water Resour. Res.*, *40*, W01510, doi:10.1029/2002WR001716.
Kang, P. K., P. de Anna, J. P. Nuñes, B. Bijeljic, M. J. Blunt, and R. Juanes (2014), Pore-scale intermittent velocity structure underpinning anomalous transport through 3-D porous media, *Geophys. Res. Lett.*, *41*, 6184–6190, doi:10.1002/2014GL061475.
Kitanidis, P. K. (1994), The concept of the dilution index, *Water Resour. Res.*, *30*(7), 2011–2026, doi:10.1029/94WR00762.
OpenFOAM (2011), The open source CFD toolbox. [Available at http://www.openfoam.com.]
Orgogozo, L., F. Golfier, M. Buès, and M. Quintard (2010), Upscaling of transport processes in porous media with biofilms in non-equilibrium conditions, *Adv. Water Resour.*, *33*, 585–600.
Pereira Nunes, J. P., B. Bijeljic, and M. J. Blunt (2015), Time-of-flight distributions and breakthrough curves in heterogeneous porous media using a pore-scale streamline tracing algorithm, *Transp. Porous Med.*, *109*, 317–336, doi:10.1007/s11242-015-0520-y.
Porta, G., S. Chaynikov, M. Riva, and A. Guadagnini (2013), Upscaling solute transport in porous media from the pore-scale to dual- and multicontinuum formulations, *Water Resour. Res.*, *49*, 2025–2039, doi:10.1002/wrcr.20183.
Raeini, A. Q., M. J. Blunt, and B. Bijeljic (2012), Modelling two-phase flow in porous media at the pore-scale using the volume-of-fluid method, *J. Comput. Phys.*, *231*, 5653–5668.
Salles, J., J.-F. Thovert, R. Delannay, L. Prevors, J.-L. Auriault, and P. M. Adler (1993), Taylor dispersion in porous media. Determination of the dispersion tensor, *Phys. Fluids A*, *5*(10), 2348–76.
Scheibe, T. D., W. A. Perkins, M. C. Richmond, M. I. McKinley, P. D. J. Romero-Gomez, M. Oostrom, T. W. Wietsma, J. A. Serkowski, and J. M. Zachara (2015), Pore-scale and multiscale numerical simulation of flow and transport in a laboratory-scale column, *Water Resour. Res.*, *51*, 1023–1035, doi:10.1002/2014WR015959.
Scheven, U. M., D. Verganelakis, R. Harris, M. L. Johns, and L. F. Gladden (2005), Quantitative nuclear magnetic resonance measurements of preasymptotic dispersion in flow through porous media, *Phys. Fluids*, *17*, 117107.
Siena, M., M. Riva, J. D. Hyman, C. L. Winter, and A. Guadagnini (2014), Relationship between pore size and velocity probability distributions in stochastically generated porous media, *Phys. Rev. E*, *89*, 013018.
Soulaine, C., Y. Davit, and M. Quintard (2013), A two-pressure model for slightly compressible single phase flow in bi-structured porous media, *Chem. Eng. Sci.*, *96*, 55–70.
Spanne, P., J.-F. Thovert, C. J. Jacquin, W. B. Lindquist, K. W. Jones, and P. M. Adler (1994), Synchrotron computed microtomography of porous media: Topology and transports, *Phys. Rev. Lett.*, *73*, 2001–2004.
Swanson, R. D., A. Binley, K. Keating, S. France, G. Osterman, F. D. Day-Lewis, and K. Singha (2015), Anomalous solute transport in saturated porous media: Relating transport model parameters to electrical and nuclear magnetic resonance properties, *Water Resour. Res.*, *51*, 1264–1283, doi:10.1002/2014WR015284.
Wang, L., M. Bayani Cardenas, W. Deng, and P. C. Bennett (2012), Theory for dynamic longitudinal dispersion in fractures and rivers with Poiseuille flow, *Geophys. Res. Lett.*, *39*, L05401, doi:10.1029/GL0831.
Whitaker, S. (1999), *The Method of Volume Averaging*, Kluwer Acad., Netherlands.
Zhang, Y., D. A. Benson, and D. M. Reeves (2009), Time and space nonlocalities underlying fractional-derivative models: Distinction and review of field applications, *Adv. Water Resour.*, *32*, 561–581.